Effects of ion irradiation on microstructure of 316L stainless steel strengthened by disperse nano TiC through selective laser melting

Zhangjie Sun [a], Yuanye Xu [b], Feida Chen [a,*], Lida Shen [b], Xiaobin Tang [a,c], Liangwei Sun [d], Minyu Fan [e], Ping Huang [e]

[a] Department of Nuclear Science and Technology, Nanjing University of Aeronautics and Astronautics, Nanjing 211106, China
[b] College of Mechanical and Electrical Engineering, Nanjing University of Aeronautics and Astronautics, Nanjing 210016, China
[c] Key Laboratory of Nuclear Technology Application and Radiation Protection in Astronautics, Ministry of Industry and Information Technology, Nanjing 211106, China
[d] Key Laboratory of Neutron Physics and Institute of Nuclear Physics and Chemistry, China Academy of Engineering Physics (CAEP), Mianyang 621999, China
[e] Suzhou Nuclear Power Research Institute, Suzhou 215004, China

ABSTRACT

The manufacturing of the new generation of radiation-resistant structural materials is an extremely interesting and challenging topic in the field of additive manufacturing research. Understanding the special microstructure characteristics and the influence on the radiation resistance of these additive manufactured materials is still superficial. In this study, high-quality bulk 316L stainless steels (SSs) strengthened by dispersed nano TiC were successfully prepared by selective laser melting (SLM). The results of transmission electron micrograph and small angle neutron scattering showed that TiC existed in the matrix of 316L SSs in the form of nanoparticles with average size less than 50 nm. TiC particles were distributed inside the subgrains and on the subgrain boundaries. Smaller helium bubbles were observed after the same flux of He^{2+} ion irradiation in the case of 316L SSs with 4% TiC compared with pure SLM 316L SSs. In comparison with the case on the grain boundaries and intragranular, the helium bubbles at TiC/316L interfaces have the smallest size and the largest density. The results Nano-indentation results showed that 4% TiC doping had a remarkable inhibiting effect on irradiation-induced hardening at a low dose. This condition is because numerous interfaces of TiC/316L acted as sink/trap sites for the irradiation-induced defects.

1. Introduction

The safety of nuclear reactor structural materials for long-term service has always been the focus in the nuclear industry. However, under complex reactor operating conditions, the materials face harsh environments, such as high temperature, high pressure, intense radiation, and severe corrosion[1–3]. Materials are usually prone to element segregation[4,5], irradiated swelling[6,7], irradiated hardening[8,9], and embrittlement[10,11], resulting in the failure of structural materials. Therefore, high requirements are established for the radiation resistance of the material.

316L stainless steel (SS) has excellent plasticity, toughness, impact resistance, corrosion resistance, and low cost. It has been used for the upper and lower tube seats in pressurized water reactor fuel assembly and pressure vessel steel in sodium cooled fast reactor. 316L SS is recognized as an important candidate material for Gen-IV nuclear reactors[3,12,13]. However, 316L SS has a series of problems, such as high neutron irradiation swelling rate, insufficient high temperature strength, and large hydrogen isotope diffusion coefficient[14,15], with the severe situation of the service environment in the future advanced nuclear power systems. The condition seriously affects its service safety and stability in the extreme environment of reactor.

Dispersion strengthening of matrix materials with nano second phase is an important idea to overcome the limits of the high-temperature mechanical properties and radiation resistance of existing materials. Considering the toughness and stability of the second phase material and the matching requirements with the thermal expansion performance of the matrix material, the candidate second phase materials mainly include TiB_2, TiC, and Y_2O_3[16–19]. TiC has become the preferred reinforcing material due to its good compatibility with 316L SS and, is expected to improve the yield strength and radiation resistance of SS. TiC particles dispersed in the steel have a strong ability to capture

Table 1

Chemical compositions (wt%) of 316L SS power in this study.

	Cr	Ni	Mo	Si	Mn	C	S	P	Fe
316L SS	16.49	10.51	2.70	0.47	1.70	0.02	0.01	0.04	Bal.

Table 2

Process parameters of SLM 316L SS.

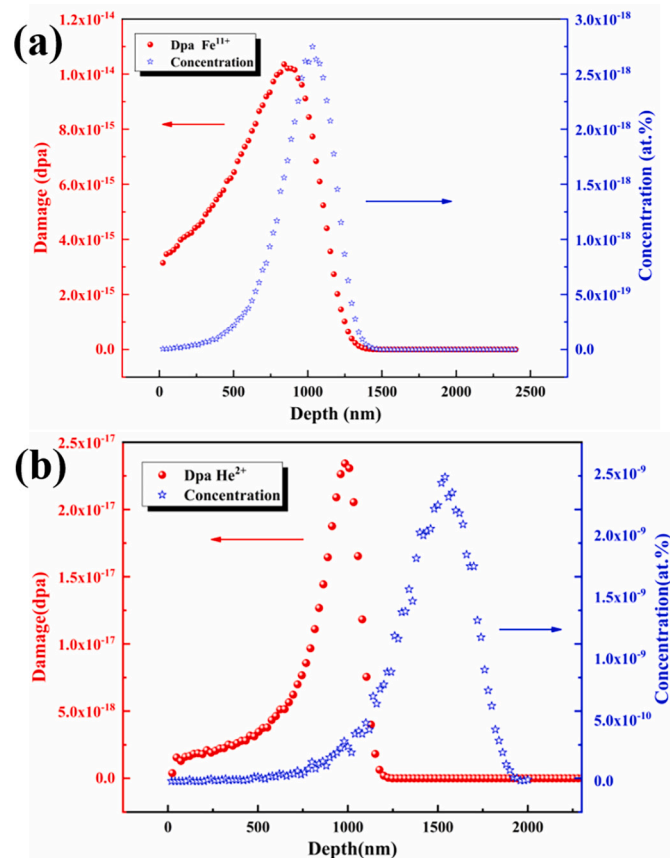| Atmosphere	Power (W)	Scanning rate (mm/s)	Line spacing (mm)	Spot diameter (μm)
Ar	190	1000	0.06	70

Fig. 1. SRIM calculated (a) Fe^{11+} and (b) He^{2+} damage profile (red line). (For interpretation of the references to colour in this figure legend, the reader is referred to the web version of this article.)

reform in the manufacturing technology of nuclear engineering components. Nuclear power giants, such as Oak Ridge Laboratory, Westinghouse Electric Company, and Framatome Company, are actively developing AM printing technology and conducting irradiation tests of AM materials in the reactor. AlMangour et al. prepared TiC/316L by SLM and systematically studied different printing strategies, preparation methods and mechanical properties. Nano TiC improves the compressive strength, yield strength and wear resistance[27–31]. In recent years, nuclear materials researchers have begun to expand the scope of AM materials from conventional materials such as 316L SS [6,32–34] and Ni-based alloys[35,36], to a new generation of radiation-resistant materials, such as oxide dispersion-strengthened steel[37,38]. However, some problems, such as particle agglomeration and insufficient density are found. At present, the technology is still in the exploratory stage. In the study of the irradiation effect of AM materials, previous studies found that AM materials have special microstructures, such as ultra-high density subgrain boundaries(SGBs)[33]. In situ Kr ion irradiation studies showed that high-density solidification cellular structures can reduce dislocation loop density[39]. Thus, cellular dislocation structure in AM 316L acts as sink/trap sites for the irradiation-induced defects[40].

On the one hand, the existence of nanoparticles in the second phase particle-reinforced steel made by AM may differ from the conventional methods, and the mechanical properties are improved[41–44]. On the other hands, the interaction between nanoparticles and SGBs leads to different radiation resistance. Research on this aspect is just beginning, and the understanding of the performance of special structure is still insufficient.

In this study, we used SLM technology to synthesize bulk and high-density TiC/316L SS. The microstructure of the material was studied by small angle neutron scattering (SANS) and transmission electron microscopy (TEM). He^{2+} and Fe^{11+} ion irradiation experiments were carried out to explore the radiation effects of the material.

2. Experiment

2.1. Material preparation

Commercial 316L powders (particle size of 30–50 μm) and TiC spherical powders (particle size of approximately 50 nm) were used as raw materials in this study. Ball milling were conducted in argon atmosphere. The doping content was 0%, 2%, and 4% (mass ratio). Powders were milled with ball-to-powder mass ratios of 5:3 and for 24 h. The chemical composition of 316L powder is shown in Table 1.

The samples were fabricated on the SLM NCL-M2120 machine with a maximum power of 300 W. The process parameters of SLM printing are listed in Table 2.

2.2. Irradiation experiments

Irradiation experiments were conducted on the 320 kV Platform of Modern Physics Research Institute of Chinese Academy of Sciences. 316L SSs were processed into rectangular pieces of 15 mm (length) × 7.5 mm (width) × 1 mm (thickness) by wire cutting. When the vacuum degree of the chamber reaches 5×10^{-6} Pa, 540 keV He^{2+} ions to fluences of 8.88×10^{15} ions/cm^2 and 2.22×10^{17} ions/cm^2 and 3 MeV Fe^{11+} ions to fluences of 1.93×10^{14} ions/cm^2 and 4.83×10^{15} ions/cm^2 were injected at 500 °C, corresponding to approximately 0.2 and 5 dpa. The corresponding profile of the irradiation-induced damage and the implanted atom concentration were calculated on SRIM-2013 at the
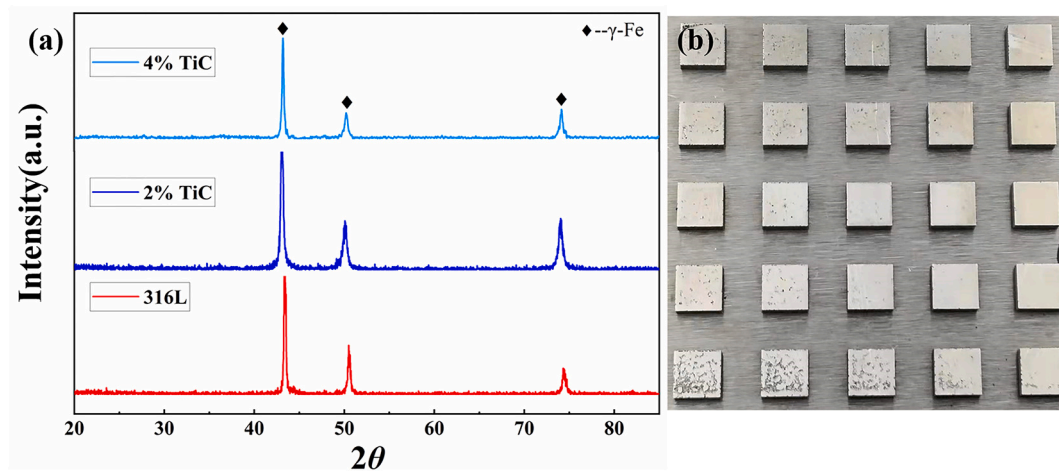
hydrogen and its isotopes, which can greatly inhibit the permeation and diffusion of hydrogen isotopes in the material[20,21]. Moreover, TiC particles are dispersed in the SS matrix, forming effective pinning on the grain boundaries GBs, thereby improving its high-temperature strength and high-temperature creep resistance, and the strengthening ability increases with the decreasing of the matrix grain size[22]. Researchers have found that the high-density TiC/SS interface can be used as a sink to capture point defects or helium atoms generated by irradiation, which can promote the annihilation of radiation-induced defects, and inhibit the formation and growth of helium bubbles[23–25]. However, reasonably controlling the size and density of the particles is necessary to achieve strengthening. At present, this condition remains challenging in processing and manufacturing.

Additive manufacturing technology (AM), including selective laser melting (SLM), has a high level of design-flexibility and rapid prototyping of complex structural parts[26]. AM has initiated a wave of

Fig. 2. (a) XRD patterns of the three bulk samples. (b) 2% TiC/316L SS bulk samples.

Table 3
FWHM of (111) austenite diffraction peak in three samples.

Samples	2θ (°)	FWHM (rad)
0% TiC/316L	43.345	0.222
2% TiC/316L	43.200	0.254
4% TiC/316L	43.059	0.313

Quick Kinchin-Pease mode. The influence of TiC content on SRIM results is insignificant, and only the result of 2 wt% TiC/316L SS is shown in Fig. 1. The ranges of Fe^{11+} and He^{2+} ions are approximately 1480 and 1296 nm, respectively.

and ion implantation profile (blue line).

2.3. Phase and microstructure characterization

The phase structures of the milled powders and polished samples were characterized through X-ray diffraction (XRD) at 40 kV voltage and 40 mA current. The scanning speed was set to 5°/min. At present, TEM and SANS are the main experimental methods used to characterize the size and distribution of the second phase in SS. Although the TEM results are intuitive, the observation area is extremely small, and the results have no statistical significance. SANS was used to measure the size and distribution of TiC particles in the matrix. SANS measurements were conducted on a SANS-Suanni spectrometer at China Mianyang Research Reactor (CMRR)[45]. The samples for SANS investigation were prepared as polished bulk with approximately 1 cm^2 in surface area and 1 mm thickness.

The microstructure of powder samples and bulk samples were observed by SEM (TESCAN LYRA3 GM) at a working voltage of 20 kV. Composition analysis was conducted through energy dispersive X-ray spectroscopy (EDS). Thin samples were observed through TEM (FEI Talos F200X operated at 200 kV with two-beam conditions). TEM samples were prepared by using electrolysis double spray instrument (MTP-1A) and focus ion beam (FIB, Helios G4 UX, Shanghai Institute of Optics and Fine Mechanics, CAS). The samples of electrolysis double spray were ground to 40–50 μm with sandpaper, and the circular flakes with 3 mm diameter were cut out. Perchlorate ethanol mixed solution (6%) was added. At −25 °C, the samples were broken down by electrolysis (70 V voltage and 100 mA current) to obtain the thin area for TEM observation.

2.4. Irradiation effects

Nanoindentation tests were performed using a diamond Berkovich indenter in a Nano Indenter G200 (Agilent Technologies) with a continuous stiffness measurement (CSM) mode. The high-frequency harmonic force was added to the quasi-static basis by the continuous stiffness measurement (CSM), to obtain the values of load, hardness and elastic modulus of the material at different depths.

3. Results and discussion

3.1. Microstructure and phase composition

After ball milling all the powder for 24 h, SLM technology was used to print the TiC/316L SS with different doping amount. As shown in Fig. 2(b), 2% TiC/316L SS bulk samples were prepared. The printed samples have a good density (>98%) measured by Archimedes drainage method. It is worth mentioning that the relationship between the forming quality and the process parameters, such as laser power, scan speed, hatch sapcing and layer thickness, has been studied and optimized to reach near full density[46–48]. The XRD patterns of the three bulk samples are shown in Fig. 2(a). Obvious diffraction peaks of austenite γ-Fe were found in the three samples, but no diffraction peak of TiC was observed. All the samples maintain single-phase structure of austenite FCC. Among the three samples, the diffraction peaks of (111) γ-Fe with 2θ of approximately 43.5° are compared and the results of full width at half maximum (FWHM) are shown in Table 3. The diffraction peaks shift to the left after doping. This condition was because the trace elements C and Ti were dissolved in the crystal lattice during SLM. The introduction of TiC particles increased the residual stress of the sample. In accordance with Scherrer formula, the increase in FMHW indicated the decrease in grain size of the 316L SS[49]. With the increase in TiC doping content, the refinement effect strengthened. Proving whether TiC particles refine the grain is necessary.

TEM observation was conducted to further observe the distribution of TiC particles in matrix materials. The TEM patterns of 2% TiC/316L SS are shown in Fig. 3. The results showed that no agglomeration phenomenon was observed in the samples, and the nanoparticles with the size below 50 nm were square. The particles were dispersed inside the subgrains and on the SGBs, indicating that the dispersion effect of ball milling was remarkable. As shown in Fig. 3(a), the enrichment of Cr was obvious, Ni was slightly enriched, and Fe was depleted. In SLM, the crystal grew rapidly. Insufficient diffusion of large radius atom, such as Cr, or heavy elements, such as Mo and Ni, caused the enrichment phenomenon at the SGBs due to the extremely high cooling rate and short alloying time. In the EDS diagram, the elements C and Ti did not correspond to each other perfectly. This condition is because the element C is unremarkable under EDS and is interfered by many conditions. However, the square particles were confirmed to be TiC, as shown in Figs. 3(b) and 3(c) from the high resolution of TiC particles.
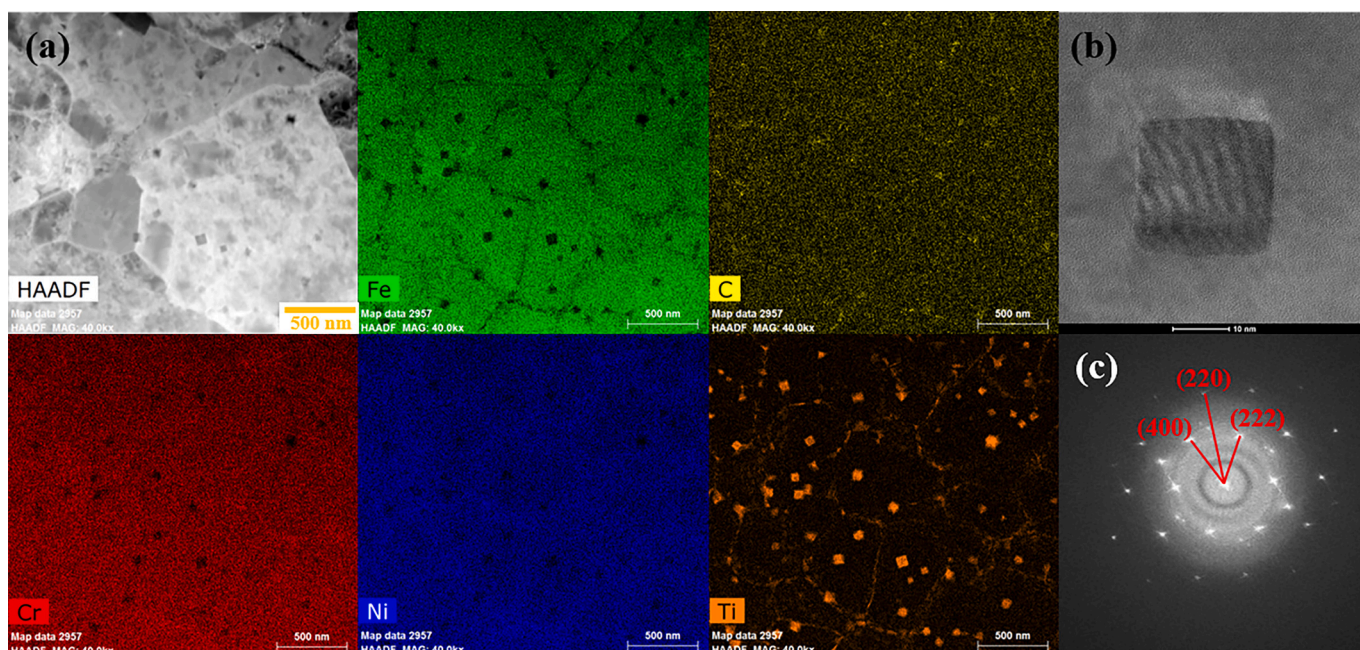
Fig. 3. TEM images of 2% TiC/316L SS: (a) STEM-EDS diagram. (b) high-resolution diagram of TiC particles. (c) SAED diagram corresponding to (b).
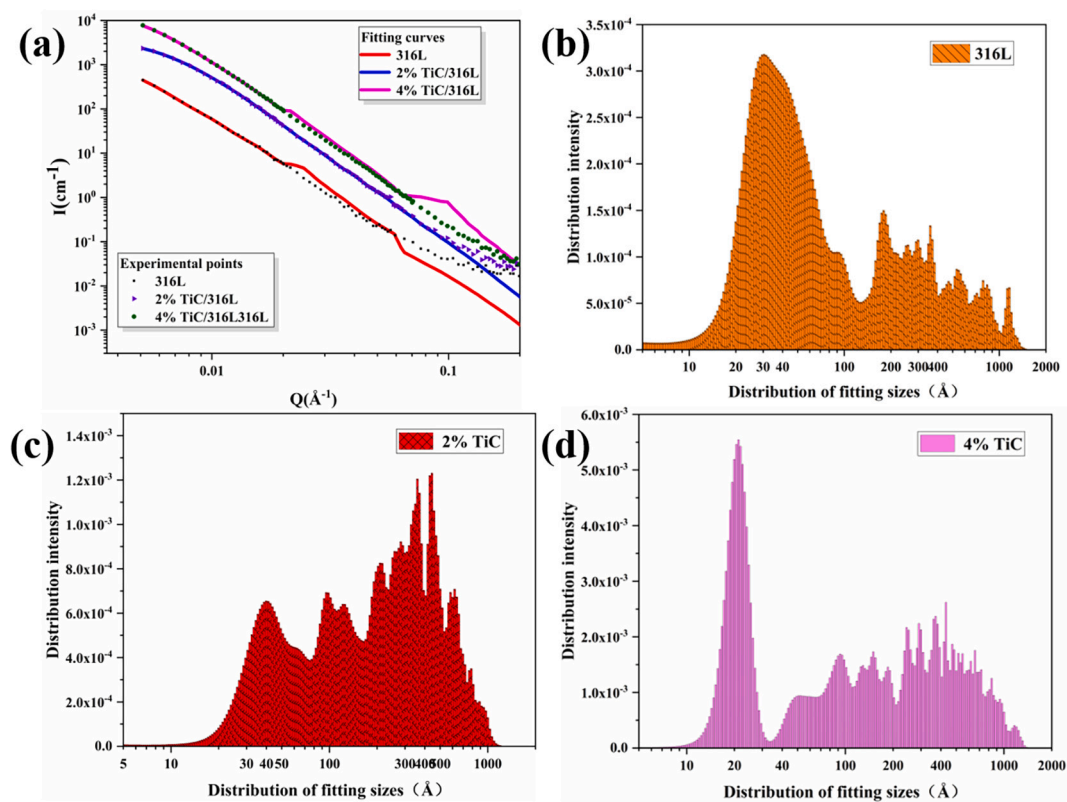

Fig. 4. SANS results of three samples. (a) Scattering intensity and scattering vector *I–Q* curve. (b), (c), and (d) are the fitting results of 316L, 2% TiC/316L, and 4% TiC/316L, respectively.

The diffraction spots of selected area electron diffraction (SAED) were calibrated and the crystal orientations corresponding to TiC lattice were found, where (hkl) was (220), (222), and (400).

SANS is an excellent method used to further investigate the statistical feature of the TiC-dispersed phase size and the density in samples with different TiC contents. In the SANS experiment, only the coherent elastic

interaction between neutron beam and sample was considered. The size of scattering vector remains unchanged, but the direction changes before and after small angle scattering. Thus, a scattering vector transfer Q is found, where $Q = \frac{4\pi}{\lambda}sin\theta$, λ is the wavelength, and 2θ is the scattering angle. In this work, a spherical model was used to fit the nanoparticles. The scattering intensity and scattering vector *I–Q* curves of three
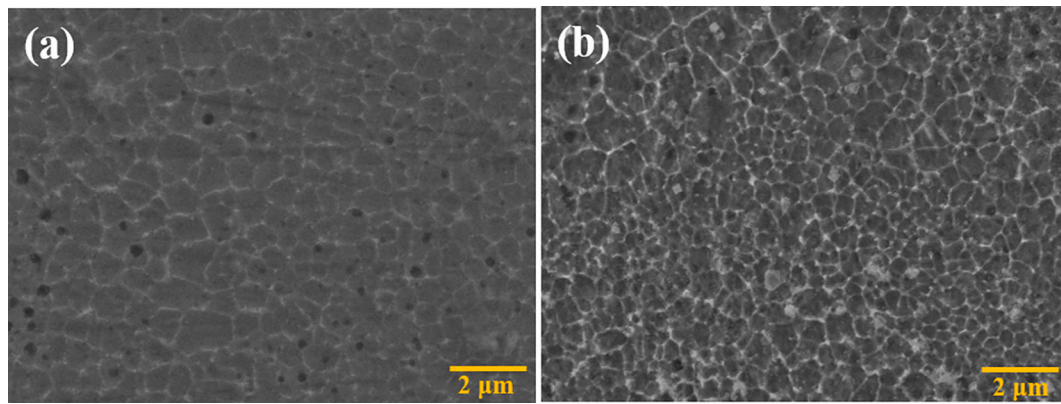
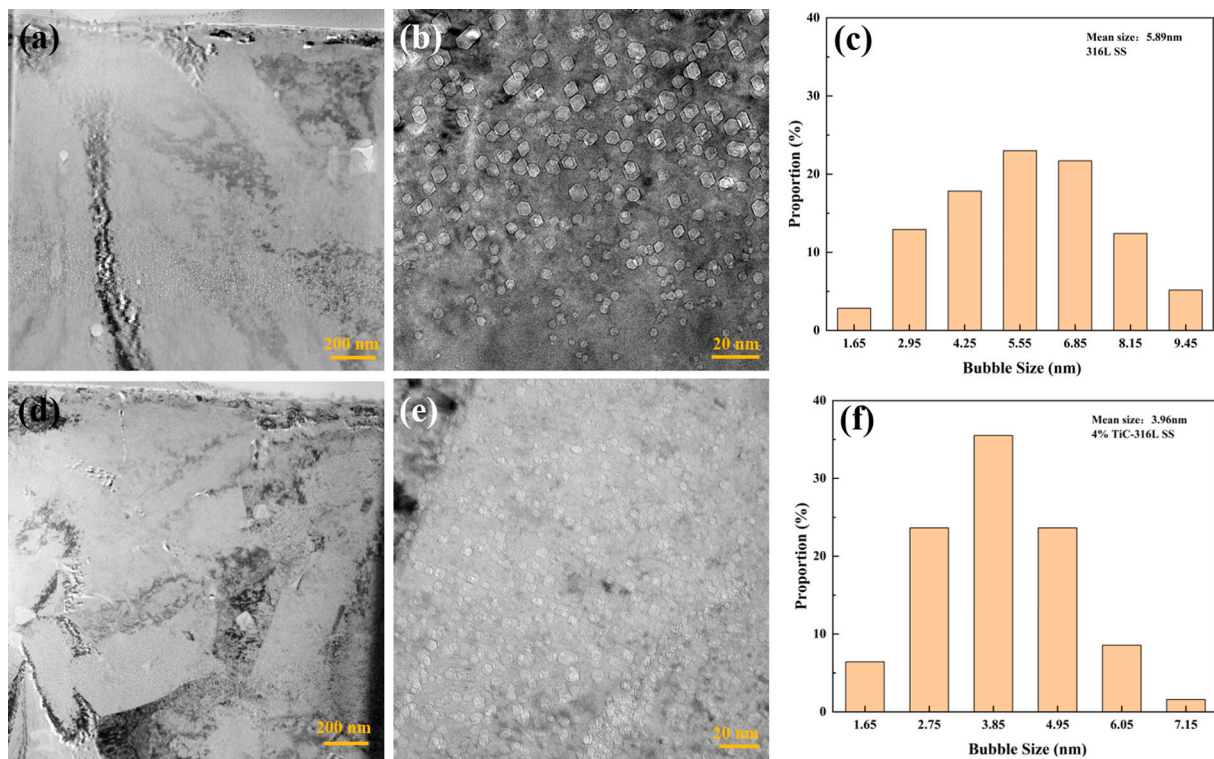**Fig. 5.** SEM images of the two doped samples.

Fig. 6. (a), (d) are the cross section TEM micrographs of SLM 316L SS and 4% TiC/316L SS, (b), (e) are the enlarged images of the dense area of helium bubbles, (c), (f) are the statistical results of helium bubble size and distribution.

samples are shown in Fig. 4(a). Maximum entropy method was used to fit the size and strength curve of the secondary phase particles, as shown in Figs. 4(b), 4(c), and 4(d).

Different structural information can be obtained from different Q regions. At low Q regions ($Q < 0.01$ Å^{-1}), the intensity reflects the information on geometry and size of the sample. At high Q ($Q > 0.01$ Å^{-1}) regions, the intensity reflects the information on surface roughness and crystallinity of the sample[50]. Many nanoscale secondary particles were existed in the 316L sample, which were nano silicon oxides[33], but the density is one order of magnitude lower than that of TiC. Whether at low Q or high Q region, the intensity increased with the increase in TiC doping amount. Although TiC particles were square, the spherical model was selected in this study due to the limitation of fitting model, thereby affecting the results. The size of the second phase ranged from 10 Å to 1000 Å through fitting. When doping 2% TiC, the size of nanoparticles was mostly 30–40 nm. At 4% TiC doping, ultrafine particles with the size of 2 nm were found in the matrix.

The SEM images of the two doped samples are shown in Fig. 5, where the cellular subgrain structure can be clearly observed, which is a unique structural feature of SLM materials. The size of subgrains and the distribution of samples were calculated on Nano Measurer 1.2 software. At least 250 cellular subgrains were counted for each sample to reduce the error. The average size of subgrains with 2% and 4% TiC were 0.72 and 0.51 μm, respectively. The grains were refined after doping TiC nanoparticles. A large number of nano particles were dispersed on the SGBs, corresponding to the results of SANS. Apart from TiC, the doped ceramic particles induce the precipitation of secondary phase in the matrix when doping 4% TiC. In accordance with previous SLM study, the precipitates may be $M_{23}C_6$ carbides[51].

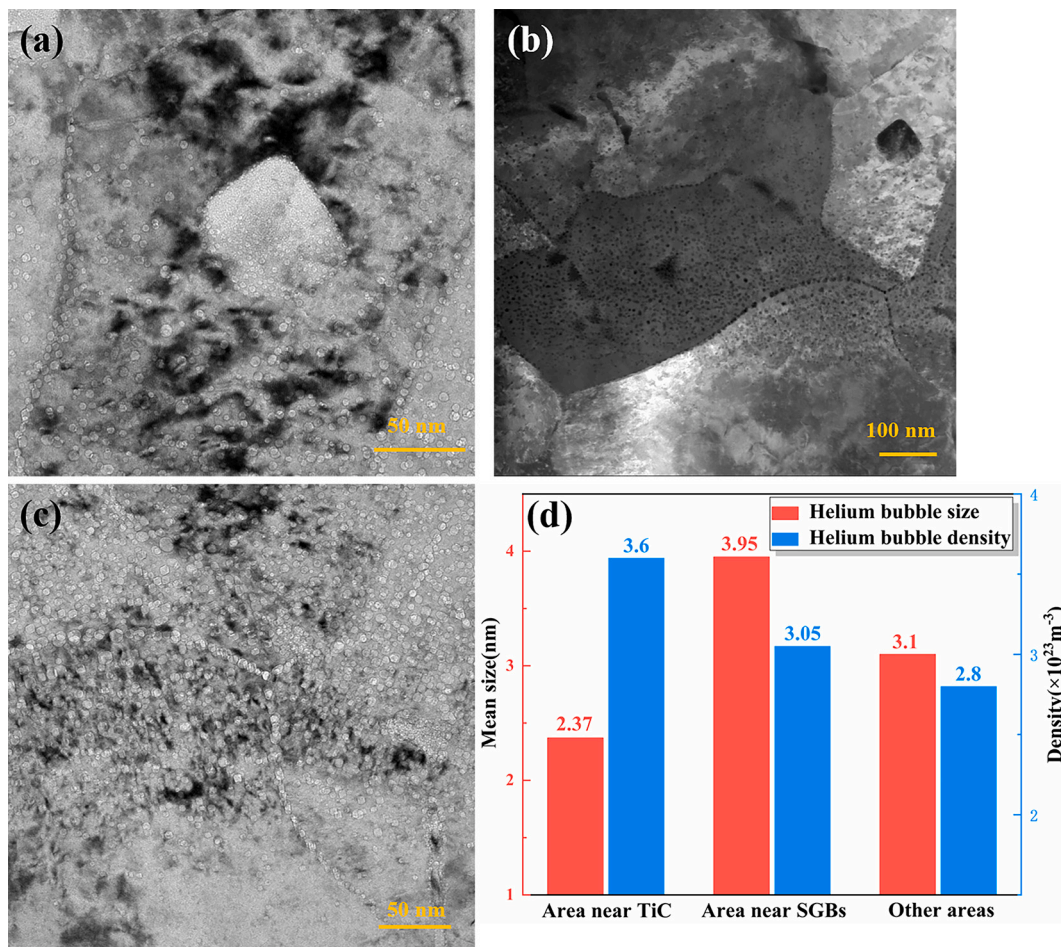(a) 2% TiC/316L SS; (b) 4% TiC/316L SS.

Fig. 7. TEM images of 4% TiC/316L SS. (a) Helium bubbles around TiC. (b) Bubbles appeared as black dots in the overfocus condition. (c) Bubbles appeared as white dots under the underfocus condition. (d) Statistical chart of helium bubble size and density in three different regions at the same depth.
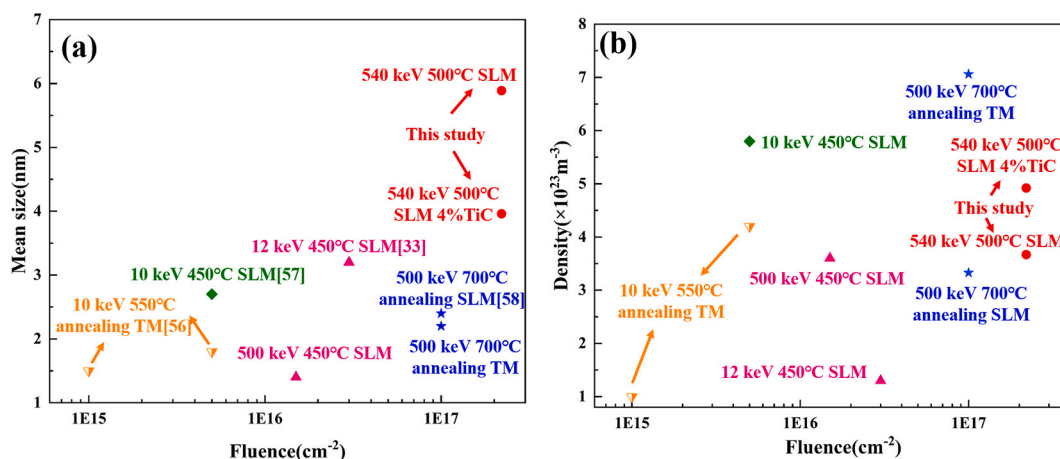

Fig. 8. Statistical chart of fluence and helium bubble (a) size and (b) density of SLM and TM 316L SS under different irradiation conditions.

3.2. Irradiation effects

3.2.1. Helium bubbles

In the process of He^{2+} ion irradiation, vacancies and other defects were introduced. These vacancies migrated and combined with helium atoms to form helium bubbles. TEM samples were sliced by FIB technique with a thickness of approximately 50 nm.

The TEM images of the samples with 0% and 4% TiC under He^{2+}

irradiation dose of 5 dpa at 500 °C are shown in Fig. 6. No helium bubbles appeared on the surface of the two samples. The helium bubble appeared at the range of 435–1328 nm away from the surface of 316L SS sample. The densest region of helium bubbles was 1000–1250 nm, which was similar to the simulation results of SRIM. The helium bubble range and the densest range of 4% TiC/316L SS are 448–1367 and 1026–1310 nm. The helium bubbles in the most concentrated area of the two samples (approximately 1050 nm from the surface) were
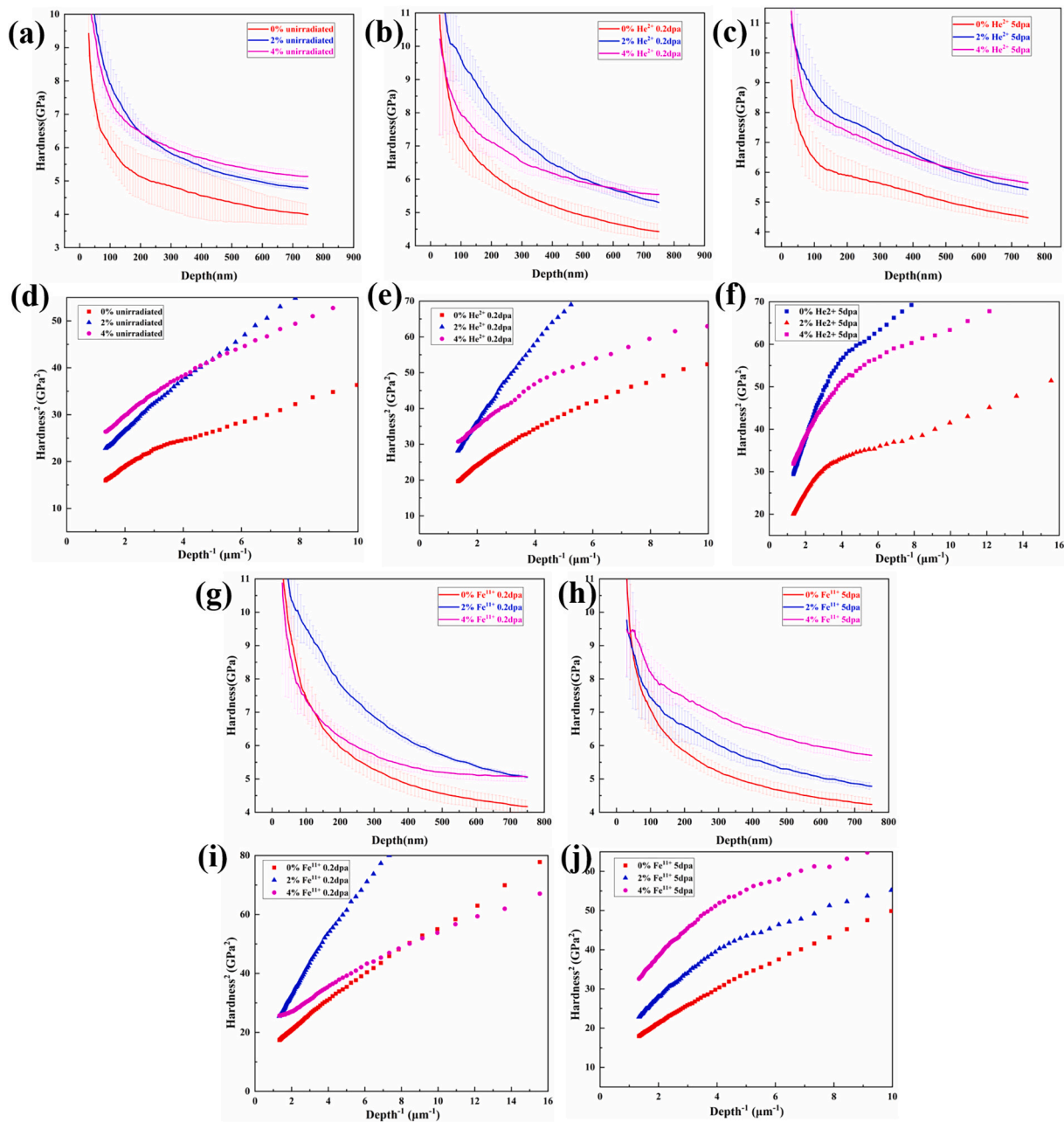
Fig. 9. Average nanoindentation hardness versus the indentation depth of 0% TiC, 2% TiC, and 4% TiC (a) before irradiation, (b) after He^{2+} 0.2 dpa irradiation, (c) after He^{2+} 5 dpa irradiation, (g) after Fe^{11+} 0.2 dpa irradiation, and (h) after Fe^{11+} 5 dpa irradiation. (d)–(f) and (i)–(j) are the curves of H^2–$1/D$ for the average nanoindentation hardness of all the samples.

Table 4
Hardness (GPa) of three materials calculated by the Nix–Gao model.

Samples	Unirradiated	Fe^{11+} 0.2 dpa	Fe^{11+} 5 dpa	He^{2+} 0.2 dpa	He^{2+} 5 dpa
	Hardness (GPa)				
TiC-0%	3.28	4.26	4.24	4.85	5.17
TiC-2%	4.1	5.10	5.55	5.92	6.66
TiC-4%	4.59	5.44	6.48	5.95	6.83

Table 5
Hardening rate of three materials.

Samples	Fe^{11+} 0.2 dpa	Fe^{11+} 5 dpa	He^{2+} 0.2 dpa	He^{2+} 5 dpa
	Hardening rate (%)			
TiC-0%	29.88	29.27	47.87	57.62
TiC-2%	24.40	35.37	44.39	62.44
TiC-4%	18.52	41.18	29.63	48.8

statistically analyzed. The comparison results are shown in Figs. 6(c) and 6(f). The average size of the helium bubbles with 0% and 4% TiC are 5.89 nm and 3.96 nm. The number density increases from 3.67×10^{23} m^{-3} to 4.92×10^{23} m^{-3}. Therefore, the size and density of He bubbles

changed with the addition of TiC particles.

The area near TiC, the area near SGBs, and other areas at the same depth were observed through TEM to further understand the influence of TiC and SGBs on helium bubbles. As shown in Fig. 7, the helium bubbles

around TiC particles were significantly the densest and smallest in size compared with other areas, where the mean size was 2.37 nm, and the density was 3.6×10^{23} m^{-3}. Generally, the defect trapping strength of the phase boundary is higher than that of the grain boundary. The interface between TiC and 316L can absorb a large number of helium atoms to form pressurized helium bubbles, resulting in more helium bubbles around TiC. The region of SGBs is presented in overfocus and underfocus conditions in Figs. 7(b) and 7(c) for better identification of helium bubbles. A larger density of bubbles appeared to be near the SGBs than other areas in matrix materials. SGBs can be treated as preferential trap sites for He atoms and irradiation-induced defects due to the low migration energy of interstitial He atoms, causing them to quickly move to GBs[52,53]. Helium bubbles were adsorbed at the interface between the TiC nanoparticles and the 316L SS. The density of helium bubbles around the nanoparticles is higher than others, but the size is smallest. A large number of helium bubbles accumulated in the material leads to radiation-induced swelling. The degree of radiation-induced swelling of the material is evaluated in terms of the swelling rate. The helium bubbles are approximately spherical, and the calculation formula is as follows[54]:

$$S = \frac{\Delta V}{V} \times 100\% = \frac{\Sigma \frac{4}{3}\pi r^3}{V} \times 100\%$$

where S is the swelling rate, ΔV is the volume of helium bubbles, V is the volume of observation area, and r is the radius of helium bubbles. The swelling rate of SLM 316L SS is 5.29% and that of SLM 4% TiC/316L SS is 2.09%. The interface between TiC/316L hindered the growth and diffusion of helium bubbles, and significantly reduced the swelling rate of the material, which is the same as conclusion of the previous researchers[23,55].

The corresponding statistical graphs from some previous related reports[33,56–58] are shown in Fig. 8. to compare the size and density of helium bubbles in 316L SS under different preparation processes and different irradiation conditions. General conclusions can be summarized. With the increase in the radiation fluence, the size and density of helium bubbles increase. SLM 316L has a lower helium bubble density than the traditional manufactured (TM) 316L, showing better radiation resistance. The annealed SLM 316L SS forms a relatively loose dislocation network that usually reduces the density of helium bubbles. In this study, the size of the helium bubble in SLM 316L SS can be further reduced by doping 4% TiC.

3.2.2. Radiation hardening

The nanoindentation results are shown in Fig. 9. The geometry of indenter, strain rate, and surface finish of sample greatly influence the data of the first 80 nm, resulting in anti-nano indentation size effect (AISE). The condition increases the nano hardness with the indentation depth. Therefore, the data of less than 80 nm depth were discarded. Fig. 9(a) shows that the hardness of the samples increases with the doping content of TiC before irradiation. As shown in Fig. 9, the hardness gradually decreases with the increase in depth after 100 nm and tends to be flat. This phenomenon is called the indentation size effect (ISE). This effect can be explained by the geometric necessary dislocation theory model proposed by Nix and Gao[59].

$$H = H_0\sqrt{1 + h^*/h,}$$

where H is the hardness, H_0 is the hardness at limit infinite depth, h is the indentation depth of the indenter, and h^* is the characteristic length, which is determined by the shape of the indenter and the type of material[59,60]. The method proposed by Kasada et al. was used to draw the relationship curve between H^2 (the square of hardness) and $1/D$ (the reciprocal of indentation depth)[61] to obtain the real hardness of materials quantitatively. The curves of the irradiated samples are bilinear, whereas the "H^2-$1/D$" curves bend downward at 300–400 nm due to unirradiated softer substrate, which is similar to the results of other

studies[58]. The hardnesses of the three materials under different irradiation conditions are given in Tables 4 and 5. All the samples have different degrees of radiation hardening. Under the same irradiation damage, the radiation hardening rate caused by He^{2+} is higher than that of Fe^{11+} irradiation; this condition is possibly due to the influence of He bubbles. In addition to point defects such as vacancies and interstitial atoms, He impurities and vacancies will also form He-Vacancy clusters, resulting in worse mobility and greater obstacles to dislocation slip, so the hardening phenomenon by He^{2+} irradiation is more obvious. Under low-dose irradiation conditions, the hardening rate of the samples decreases with the increase in the doping content of TiC. The sample with 4% TiC still has a lower irradiation hardening rate under He^{2+} irradiation dose of 5 dpa. From the results of this study, 4% TiC can inhibit radiation hardening, whereas TiC may fail under high dose.

4. Conclusion

In this work, bulk and high-density nano TiC dispersion strengthened 316L SSs were prepared by using SLM technology. High-quality manufacturing can be achieved by directly mixing nano TiC powders into 316L SS powder for ball milling and printing. The TEM and SANS results show that TiC is uniformly distributed in 316L SS. The addition of TiC can refine the SGBs.

The microstructure and radiation effects of SLM TiC/316L SS were studied under Fe^{11+} and He^{2+} irradiation conditions. In comparison with 0% TiC doping, 4% TiC/316L SS samples exhibited smaller-sized helium bubbles and increased helium bubble densities. Specifically, the helium bubbles around TiC particles were significantly the densest and smallest in size. SLM 4% TiC/316L SS effectively inhibited hardening at low dose.

Overall, SLM TiC/316L SS exhibited excellent radiation resistance, confirming its suitability for the intended applications. However, in-depth studies, including the influence of TiC particles on the formation and growth of helium bubbles, should be conducted and observed by in situ TEM.

Declaration of Competing Interest

There are no conflicts of interest to declare.

Data availability

The raw/processed data required to reproduce these findings cannot be shared at this time due to technical or time limitations.

References

[1] S.J. Zinkle, J.T. Busby, Structural materials for fission & fusion energy, Mater. Today (2009), https://doi.org/10.1016/S1369-7021(09)70294-9.
[2] K. Jin, C. Lu, L.M. Wang, J. Qu, W.J. Weber, Y. Zhang, H. Bei, Effects of compositional complexity on the ion-irradiation induced swelling and hardening in Ni-containing equiatomic alloys, Scr. Mater. (2016), https://doi.org/10.1016/j.scriptamat.2016.03.030.
[3] S.J. Zinkle, G.S. Was, Materials challenges in nuclear energy, Acta Mater. (2013), https://doi.org/10.1016/j.actamat.2012.11.004.
[4] S. Watanabe, N. Sakaguchi, N. Hashimoto, M. Nakamura, H. Takahashi, C. Namba, L. N.q, Radiation-induced segregation accompanied by grain boundary migration

in austenitic stainless steel, J. Nucl. Mater. (1996), https://doi.org/10.1016/S0022-3115(96)00433-3.

[5] W. Kesternich, A. Garcia-Borquez, Inversion of the radiation-induced segregation behaviour at grain boundaries in austenitic steel, Scr. Mater. (1997), https://doi.org/10.1016/S1359-6462(97)00004-3.

[6] J. Lin, F. Chen, X. Tang, J. Liu, S. Shen, G. Ge, Radiation-induced swelling and hardening of 316L stainless steel fabricated by selected laser melting, Vacuum (2020), https://doi.org/10.1016/j.vacuum.2020.109183.

[7] C. Zheng, D. Kaoumi, Radiation-induced swelling and radiation-induced segregation & precipitation in dual beam irradiated Ferritic/Martensitic HT9 steel, Mater. Charact. (2017), https://doi.org/10.1016/j.matchar.2017.10.019.

[8] X. Liu, R. Wang, A. Ren, J. Jiang, C. Xu, P. Huang, W. Qian, Y. Wu, C. Zhang, Evaluation of radiation hardening in ion-irradiated Fe based alloys by nanoindentation, J. Nucl. Mater. (2014), https://doi.org/10.1016/j.jnucmat.2013.09.026.

[9] X. Hu, T. Koyanagi, M. Fukuda, N.A.P.K. Kumar, L.L. Snead, B.D. Wirth, Y. Katoh, Irradiation hardening of pure tungsten exposed to neutron irradiation, J. Nucl. Mater. (2016), https://doi.org/10.1016/j.jnucmat.2016.08.024.

[10] G.R. Odette, G.E. Lucas, Embrittlement of nuclear reactor pressure vessels, JOM (2001), https://doi.org/10.1007/s11837-001-0081-0.

[11] R.L. Klueh, K. Shiba, M.A. Sokolov, Embrittlement of irradiated ferritic/martensitic steels in the absence of irradiation hardening, J. Nucl. Mater. (2008), https://doi.org/10.1016/j.jnucmat.2008.04.002.

[12] K.L. Murty, I. Charit, Structural materials for Gen-IV nuclear reactors: Challenges and opportunities, J. Nucl. Mater. (2008), https://doi.org/10.1016/j.jnucmat.2008.08.044.

[13] P. Yvon, F. Carré, Structural materials challenges for advanced reactor systems, J. Nucl. Mater. (2009), https://doi.org/10.1016/j.jnucmat.2008.11.026.

[14] O.K. Chopra, A.S. Rao, A review of irradiation effects on LWR core internal materials - Neutron embrittlement, J. Nucl. Mater. (2011), https://doi.org/10.1016/j.jnucmat.2011.02.059.

[15] S.A. Fabritsiev, Structural and Functional Materials: Selection Criteria and Radiation Characteristics, in: Fundam, Magn. Thermonucl. React. Des., 2018 https://doi.org/10.1016/b978-0-08-102470-6.00013-5.

[16] A. Kimura, W. Han, J.E. Je, K. Yabuuchi, R. Kasada, Oxide dispersion strengthened steels for advanced blanket systems, Plasma Fusion Res (2016), https://doi.org/10.1585/pfr.11.2505090.

[17] F.M. Shamsudin, S. Radiman, Y. Abdullah, N.A. Hamid, The effect of annealing to the hardness of high Y2O3-oxide dispersion strengthened ferritic steels, Sains Malaysiana (2018), https://doi.org/10.17576/jsm-2018-4701-22.

[18] Z. Kulikowski, A. Wisbey, T.M.T. Godfrey, P.S. Goodwin, H.M. Flower, Mechanical properties of high performance lightweight steels, in: Mater, Sci. Technol. (2000), https://doi.org/10.1179/026708300101508702.

[19] Y. Zhang, H. Qi, Y. Qu, C. Li, Q. Lv, Z. Li, R. Li, B. Tan, C. Tian, S. Nie, The effect of TiC addition on the microstructure and mechanical properties of Al0.6CrFe2Ni2 high entropy alloys, SN Appl. Sci. (2020), https://doi.org/10.1007/s42452-020-2306-2.

[20] D. Pérez Escobar, E. Wallaert, L. Duprez, A. Atrens, K. Verbeken, Thermal desorption spectroscopy study of the interaction of hydrogen with TiC precipitates, Met. Mater. Int. (2013), https://doi.org/10.1007/s12540-013-4013-7.

[21] T. Depover, K. Verbeken, The effect of TiC on the hydrogen induced ductility loss and trapping behavior of Fe-C-Ti alloys, Corros. Sci. (2016), https://doi.org/10.1016/j.corsci.2016.07.013.

[22] F. Akhtar, S.J. Guo, Microstructure, mechanical and fretting wear properties of TiC-stainless steel composites, Mater. Charact. (2008), https://doi.org/10.1016/j.matchar.2006.10.021.

[23] W. Kesternich, J. Rothaut, Reduction of helium embrittlement in stainless steel by finely dispersed TiC precipitates, J. Nucl. Mater. (1981), https://doi.org/10.1016/0022-3115(82)90705-X.

[24] M. Terasawa, H. Kurishita, T. Sakamoto, M. Niibe, H. Takahashi, S. Nishikawa, A. Yamamoto, M. Yamashita, T. Mitamura, T. Yamasaki, M. Kawai, Fabrication and characterization of fine-grained 316L steel with 2.0 mass% TiC, J. Nucl. Sci. Technol. (2016), https://doi.org/10.1080/00223131.2016.1175390.

[25] Y.J. Zheng, T. Yamasaki, M. Terasawa, T. Mitamura, T. Fukami, Formation of ultra-fine grained SUS316l steels by ball-milling and their mechanical properties after neutron irradiation, in: Mater, Sci. Forum, 2003, https://doi.org/10.4028/www.scientific.net/msf.426-432.1065.

[26] L. Thijs, F. Verhaeghe, T. Craeghs, J. Van Humbeeck, J.P. Kruth, A study of the microstructural evolution during selective laser melting of Ti-6Al-4V, Acta Mater. (2010), https://doi.org/10.1016/j.actamat.2010.02.004.

[27] B. AlMangour, D. Grzesiak, Jenn-MingYang, Selective laser melting of TiC reinforced 316L stainless steel matrix nanocomposites: Influence of starting TiC particle size and volume content, Mater. Des. (2016), https://doi.org/10.1016/j.matdes.2016.05.018.

[28] B. AlMangour, D. Grzesiak, J.M. Yang, In-situ formation of novel TiC-particle-reinforced 316L stainless steel bulk-form composites by selective laser melting, J. Alloys Compd. (2017), https://doi.org/10.1016/j.jallcom.2017.01.149.

[29] B. AlMangour, D. Grzesiak, T. Borkar, J.M. Yang, Densification behavior, microstructural evolution, and mechanical properties of TiC/316L stainless steel nanocomposites fabricated by selective laser melting, Mater. Des. (2018), https://doi.org/10.1016/j.matdes.2017.10.039.

[30] B. AlMangour, M.S. Baek, D. Grzesiak, K.A. Lee, Strengthening of stainless steel by titanium carbide addition and grain refinement during selective laser melting, Mater. Sci. Eng. A (2018), https://doi.org/10.1016/j.msea.2017.11.126.

[31] B. AlMangour, D. Grzesiak, J.M. Yang, In situ formation of TiC-particle-reinforced stainless steel matrix nanocomposites during ball milling: Feedstock powder

[32] M. Song, M. Wang, X. Lou, R.B. Rebak, G.S. Was, Radiation damage and irradiation-assisted stress corrosion cracking of additively manufactured 316L stainless steels, J. Nucl. Mater. (2019), https://doi.org/10.1016/j.jnucmat.2018.10.044.

[33] X. Sun, F. Chen, H. Huang, J. Lin, X. Tang, Effects of interfaces on the helium bubble formation and radiation hardening of an austenitic stainless steel achieved by additive manufacturing, Appl. Surf. Sci. (2019), https://doi.org/10.1016/j.apsusc.2018.10.268.

[34] M. McMurtrey, C. Sun, R.E. Rupp, C.H. Shiau, R. Hanbury, N. Jerred, R. O'Brien, Investigation of the irradiation effects in additively manufactured 316L steel resulting in decreased irradiation assisted stress corrosion cracking susceptibility, J. Nucl. Mater. (2021), https://doi.org/10.1016/j.jnucmat.2020.152739.

[35] A.N. Jinoop, C.P. Paul, S.K. Mishra, K.S. Bindra, Laser Additive Manufacturing using directed energy deposition of Inconel-718 wall structures with tailored characteristics, Vacuum (2019), https://doi.org/10.1016/j.vacuum.2019.05.027.

[36] I. Cieślik, M. Duchna, T. Płociński, E. Wyszkowska, A. Azarov, M. Zieniuk, Ion irradiation effect on the microstructure of Inconel 625 obtained by Selective Laser Melting and by the metallurgical process, Surf. Coat. Technol. (2020), https://doi.org/10.1016/j.surfcoat.2020.125952.

[37] B.M. Arkhurst, J.J. Park, C.H. Lee, J.H. Kim, Direct laser deposition of 14cr oxide dispersion strengthened steel powders using Y2O3 and HfO2 dispersoids, J. Korean Inst. Met. Mater. (2017), https://doi.org/10.3365/KJMM.2017.55.8.550.

[38] Y. Shi, Z. Lu, L. Yu, R. Xie, Y. Ren, G. Yang, Microstructure and tensile properties of Zr-containing ODS-FeCrAl alloy fabricated by laser additive manufacturing, Mater. Sci. Eng. A (2020), https://doi.org/10.1016/j.msea.2020.138937.

[39] Z. Shang, C. Fan, S. Xue, J. Ding, J. Li, T. Voisin, Y.M. Wang, H. Wang, X. Zhang, Response of solidification cellular structures in additively manufactured 316 stainless steel to heavy ion irradiation: an in situ study, Mater. Res. Lett. (2019), https://doi.org/10.1080/21663831.2019.1604442.

[40] S. Li, J. Hu, W.Y. Chen, J. Yu, M. Li, Y. Wang, Evolution of cellular dislocation structures and defects in additively manufactured austenitic stainless steel under ion irradiation, Scr. Mater. (2020), https://doi.org/10.1016/j.scriptamat.2019.11.036.

[41] B. AlMangour, D. Grzesiak, J. Cheng, Y. Ertas, Thermal behavior of the molten pool, microstructural evolution, and tribological performance during selective laser melting of TiC/316L stainless steel nanocomposites: Experimental and simulation methods, J. Mater. Process. Technol. (2018), https://doi.org/10.1016/j.jmatprotec.2018.01.028.

[42] W. Zhai, Z. Zhu, W. Zhou, S.M.L. Nai, J. Wei, Selective laser melting of dispersed TiC particles strengthened 316L stainless steel, Compos. Part B Eng. (2020), https://doi.org/10.1016/j.compositesb.2020.108291.

[43] S. Zhao, X. Shen, J. Yang, W. Teng, Y. Wang, Densification behavior and mechanical properties of nanocrystalline TiC reinforced 316L stainless steel composite parts fabricated by selective laser melting, Opt. Laser Technol. (2018), https://doi.org/10.1016/j.optlastec.2018.01.005.

[44] M. Ghayoor, K. Lee, Y. He, C. Hung Chang, B.K. Paul, S. Pasebani, Selective laser melting of austenitic oxide dispersion strengthened steel: Processing, microstructural evolution and strengthening mechanisms, Mater. Sci. Eng. A (2020), https://doi.org/10.1016/j.msea.2020.139532.

[45] M. Peng, L. Wen, L. Geng, G. Sun, B. Chen, C. Xie, Q. Xia, G. Yan, Q. Tian, C. Huang, B. Pang, Y. Zhang, Y. Wang, Y. Liu, W. Kang, J. Gong, A new small-angle neutron scattering spectrometer at China Mianyang research reactor, Nucl. Instruments Methods Phys. Res. Sect. A Accel. Spectrometers, Detect. Assoc. Equip. (2016), https://doi.org/10.1016/j.nima.2015.11.141.

[46] C. Cai, X. Wu, W. Liu, W. Zhu, H. Chen, J.C.D. Qiu, C.N. Sun, J. Liu, Q. Wei, Y. Shi, Selective laser melting of near-α titanium alloy Ti-6Al-2Zr-1Mo-1V: Parameter optimization, heat treatment and mechanical performance, J. Mater. Sci. Technol. (2020), https://doi.org/10.1016/j.jmst.2020.05.004.

[47] C. Cai, J.C.D. Qiu, T.W. Shian, C. Han, T. Liu, L.B. Kong, N. Srikanth, C.-N. Sun, K. Zhou, Laser powder bed fusion of Mo2C/Ti-6Al-4V composites with alternately laminated α'/β phases for enhanced mechanical properties, Addit, Manuf, 2021, https://doi.org/10.1016/j.addma.2021.102134.

[48] S. Sun, Q. Teng, Y. Xie, T. Liu, R. Ma, J. Bai, C. Cai, Q. Wei, Two-step heat treatment for laser powder bed fusion of a nickel-based superalloy with simultaneously enhanced tensile strength and ductility, Addit, Manuf, 2021, https://doi.org/10.1016/j.addma.2021.102168.

[49] F. Chang, D. Gu, D. Dai, P. Yuan, Selective laser melting of in-situ Al4SiC4 + SiC hybrid reinforced Al matrix composites: Influence of starting SiC particle size, Surf, Coatings Technol, 2015, https://doi.org/10.1016/j.surfcoat.2015.04.029.

[50] E.M. Anitas, Small-Angle Scattering from Mass and Surface Fractals, in: Complex, Biol. Phys. Syst. - Bifurcations, Solitons Fractals, 2018, https://doi.org/10.5772/intechopen.70870.

[51] D.S. Popkova, I.M. Ruslanov, A.Y. Zhilyakov, S.V. Belikov, The effect of the selective laser melting mode on second phases precipitation in 316L steel during subsequent heat treatment, in: IOP Conf, Ser. Mater. Sci. Eng., 2021 https://doi.org/10.1088/1757-899X/1029/1/012053.

[52] F. Chen, X. Tang, H. Huang, X. Li, Y. Wang, C. Huang, J. Liu, H. Li, D. Chen, Formation of He-Rich Layers Observed by Neutron Reflectometry in the He-Ion-Irradiated Cr/W Multilayers: Effects of Cr/W Interfaces on the He-Trapping Behavior, ACS Appl. Mater. Interfaces (2016), https://doi.org/10.1021/acsami.6b07419.

[53] H. Huang, X. Tang, F. Chen, J. Liu, D. Chen, Role of graphene layers on the radiation resistance of copper–graphene nanocomposite: Inhibiting the expansion

of thermal spike, J. Nucl. Mater. (2017), https://doi.org/10.1016/j.jnucmat.2017.06.023.

[54] P.P. Liu, Q. Zhan, Z.Y. Fu, Y.P. Wei, Y.M. Wang, F.M. Wang, S. Ohnuki, F.R. Wan, Surface and internal microstructure damage of He-ion-irradiated CLAM steel studied by cross-sectional transmission electron microscopy, J. Alloys Compd. (2015), https://doi.org/10.1016/j.jallcom.2015.07.177.

[55] N. Yamamoto, H. Shiraishi, H. Kamitsubo, I. Kohno, T. Shikata, A. Hishinuma, Effects of TiC distribution on the creep properties of helium injected JPCA, J. Nucl. Mater. (1985), https://doi.org/10.1016/0022-3115(85)90196-5.

[56] S. Jublot-leclerc, M. Lescoat, F. Fortuna, L. Legras, X. Li, A. Gentils, TEM study of the nucleation of bubbles induced by He implantation in 316L industrial austenitic stainless steel 466, 2015, pp. 646–652, https://doi.org/10.1016/j.jnucmat.2015.09.013.

[57] A. De Backer, G. Adjanor, C. Domain, M.L. Lescoat, S. Jublot-Leclerc, F. Fortuna, A. Gentils, C.J. Ortiz, A. Souidi, C.S. Becquart, Modeling of helium bubble nucleation and growth in austenitic stainless steels using an Object Kinetic Monte

Carlo method, Nucl. Instruments Methods Phys. Res. Sect. B Beam Interact. with Mater, Atoms, 2015, https://doi.org/10.1016/j.nimb.2014.11.110.

[58] C. Fu, J. Li, J. Bai, Y. Li, Q. Chen, G. Lei, J. Lin, Z. Zhu, Y. Meng, Effect of helium bubbles on irradiation hardening of additive manufacturing 316L stainless steel under high temperature He ions irradiation, J. Nucl. Mater. 152948 (2021), https://doi.org/10.1016/j.jnucmat.2021.152948.

[59] W.D. Nix, H. Gao, Indentation size effects in crystalline materials: A law for strain gradient plasticity, J. Mech. Phys. Solids. (1998), https://doi.org/10.1016/S0022-5096(97)00086-0.

[60] J. Li, H. Huang, G. Lei, Q. Huang, R. Liu, D. Li, L. Yan, Evolution of amorphization and nanohardness in SiC under Xe ion irradiation, J. Nucl. Mater. (2014), https://doi.org/10.1016/j.jnucmat.2014.07.036.

[61] R. Kasada, Y. Takayama, K. Yabuuchi, A. Kimura, A new approach to evaluate irradiation hardening of ion-irradiated ferritic alloys by nano-indentation techniques, Fusion Eng. Des. (2011), https://doi.org/10.1016/j.fusengdes.2011.03.073.